AJNR

MRI of the central nervous system in neonates and young children.

B C Lee, E Lipper, R Nass, M E Ehrlich, E de Ciccio-Bloom and P A Auld

MRI of the Central Nervous System in Neonates and Young Children

Benjamin C. P. Lee[1,2]
Evelyn Lipper[3]
Ruth Nass[4]
Michelle E. Ehrlich[4]
Emmanuel de Ciccio-Bloom[4]
Peter A. M. Auld[3]

Twelve normal neonates and young children, ages 32 weeks gestation to 20 months, and 22 abnormal children up to four years old had MRI scans using a 0.5 T superconducting scanner. A faint signal that was presumed to be myelin was detected in the thalami at 32 weeks; myelination of the occipital lobes was present at full term, and visible throughout the hemispheres by 8 weeks of age. Anatomical locations of congenital lesions were well demonstrated, especially in sagittal views. The signal changes of perinatal abnormalities, such as hemorrhage and hemiatrophy, were often specific. Abnormal position of the spinal cord, spinal lipomas, and other congenital lesions were also well visualized.

Central nervous system lesions in neonates and infants are currently evaluated with sonography and CT scans [1, 2]. Because of ionizing radiation, CT is used only when sonography fails to provide adequate data for clinical management. Sonography has no known biological hazards, but it is limited by technical difficulties in assessing surface structures and it often lacks specificity in evaluating white-matter abnormalities. MR promises to be valuable because of its spatial resolution and contrast sensitivity, and because there are no known hazards at currently used field strengths [3–5].

Subjects and Methods

Thirty-four children, ages newborn to 4 years old, were scanned using a Technicare (Solon, OH) 0.5 T scanner. Axial sections were routinely obtained with spin echo (SE) multislice techniques using an echo delay time (TE) of 30 msec and a repetition time (TR) of 500 msec (SE 30/500) on T1-weighted images and SE 30,60,90/2000 on T2-weighted images. Additional coronal and sagittal sections were obtained using the same techniques in selected cases. One patient was examined by the inversion recovery (IR) technique (IR 450/1500).

Scans were performed under a special experimental protocol, approved by the internal review board of our institution. The examination was limited to subjects who were capable of spontaneous, unassisted respiration. Twelve neurologically normal infants considered to be at risk from intracerebral hemorrhage were scanned after informed parental consent was obtained. Abnormal cases were selected on the basis of sonographic or CT findings. All patients were sedated with chloral hydrate. Infants were wrapped in blankets and their respiration was continuously monitored by a pediatrician or nurse, who was in attendance throughout the procedures. Total examination time was limited to 30 min for newborns and 60 min for older children.

Results

Normal

At 32 weeks gestation (one case), white matter was hypointense relative to gray matter, with slightly increased signal intensity in the thalamic regions and brainstem on SE 30/500 images (Fig. 1).
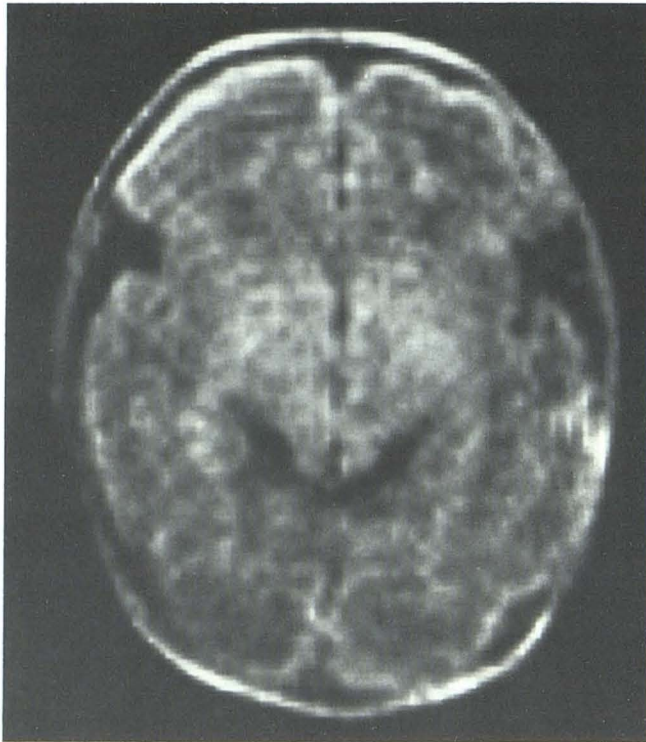
Fig. 1.—Normal infant, 32 weeks gestation. SE 30/500 image shows increased signal of thalami and internal capsules. Rest of white matter is hypointense.

At 35 weeks gestation (three cases), white matter was hypointense and there was increased signal in the internal capsule, thalamic regions, and brainstem on SE 30/500 images. Sylvian fissures and cortical sulci were visible (Fig. 2).

At 37 weeks gestation (one case), appearances were identical to those at 35 weeks (Fig. 3).

At full term (four cases), in three cases, white matter was hyperintense in all regions, markedly so in the internal capsule and the thalamic and occipital regions on SE 30/500 images (Fig. 4). In one case, increased signal was seen only in the internal capsule and thalamic regions. The sylvian fissures were smaller than in the premature infant (Fig. 5).

At 8 weeks to 20 months (three cases), white matter was hyperintense throughout on SE 30/500 images and remained unchanged between these ages (Fig. 6).

The signal of the brain was isointense in gray and white matter at all ages on SE 30,60,90/2000 images.

Abnormal

Congenital Abnormalities

Alobar holoprosencephaly (one case). Single ventricle, with no midline division, was seen best in coronal views. Associated dorsal sac was optimally shown in sagittal views (Fig. 7).

Corpus callosal agenesis (two cases). Complete absence of the corpus callosum was shown on sagittal views (Fig. 8). There was associated hypoplasia of the cerebellum and gyri in one case (Fig. 9).

Dandy-Walker anomaly (one case). Agenesis of vermis and giant fourth ventricle were seen in both sagittal and coronal views. The brainstem was also hypoplastic (Fig. 10).

Arnold-Chiari malformation (one case). Sagittal views showed the tonsillar ectopia, small posterior fossa, and configurations of the tentorium, brainstem, and third and fourth ventricles (Fig. 11).

Arachnoid cyst (one case). A large midline cyst was seen extending through an enlarged tentorial opening into the posterior fossa, causing slight compression of the upper brainstem. The signal of the fluid within the cyst was identical to that of CSF (Fig. 12).

Cerebral atrophy (one case). Cortical atrophy and dilated ventricles were seen.

Perinatal Abnormalities

Anoxia (two cases). In one case, the entire white matter was markedly hypointense on T1-weighted images (SE 30/500) compared with normal brain at the same gestation age. In another case, multiple discrete hypointense regions were seen within the basal ganglia in addition to the diffuse white-matter changes (Fig. 13).

Intracranial hemorrhage (three cases). Hemorrhage was located in the frontal and occipital lobes in two cases and was hyperintense in both T1- and T2-weighted images (Fig. 14). In the third case, hemorrhage with the same signal was seen in the quadrigeminal region, in the subdural space immediately inferior to the tentorium, and over the occipital convexities; the center of the quadrigeminal hematoma had hypointense signal (Fig. 15).

Periventricular leukoencephalomalacia (one case). Periventricular discrete cavities with signal similar to CSF were shown in the periventricular regions after a previously documented intraventricular hemorrhage (Fig. 16).

Hemiatrophy (two cases). Focal cortical atrophy with white-matter encephalomalacia was seen on T1-weighted images. T2-weighted images showed a larger region of increased signal and hemiatrophy of the ipsilateral hemisphere (Fig. 17).

Other Lesions

Tumor (three cases). A pineal tumor causing hydrocephalus was shown to be isointense on T1-weighted images and hyperintense on T2-weighted images (Fig. 18). An optic chiasm glioma was isointense on T1-weighted images and hyperintense on T2-weighted images (Fig. 19). A large craniopharyngioma occupying most of the frontal region and compressing the pituitary gland was entirely cystic and seen as hypointense on T1-weighted images and hyperintense on T2-weighted images (Fig. 20).

Tuberous sclerosis (one case). The calcified subependymal tubers were shown as isointense nodules on the walls of the lateral ventricles on T1- and T2-weighted images (Fig. 21).
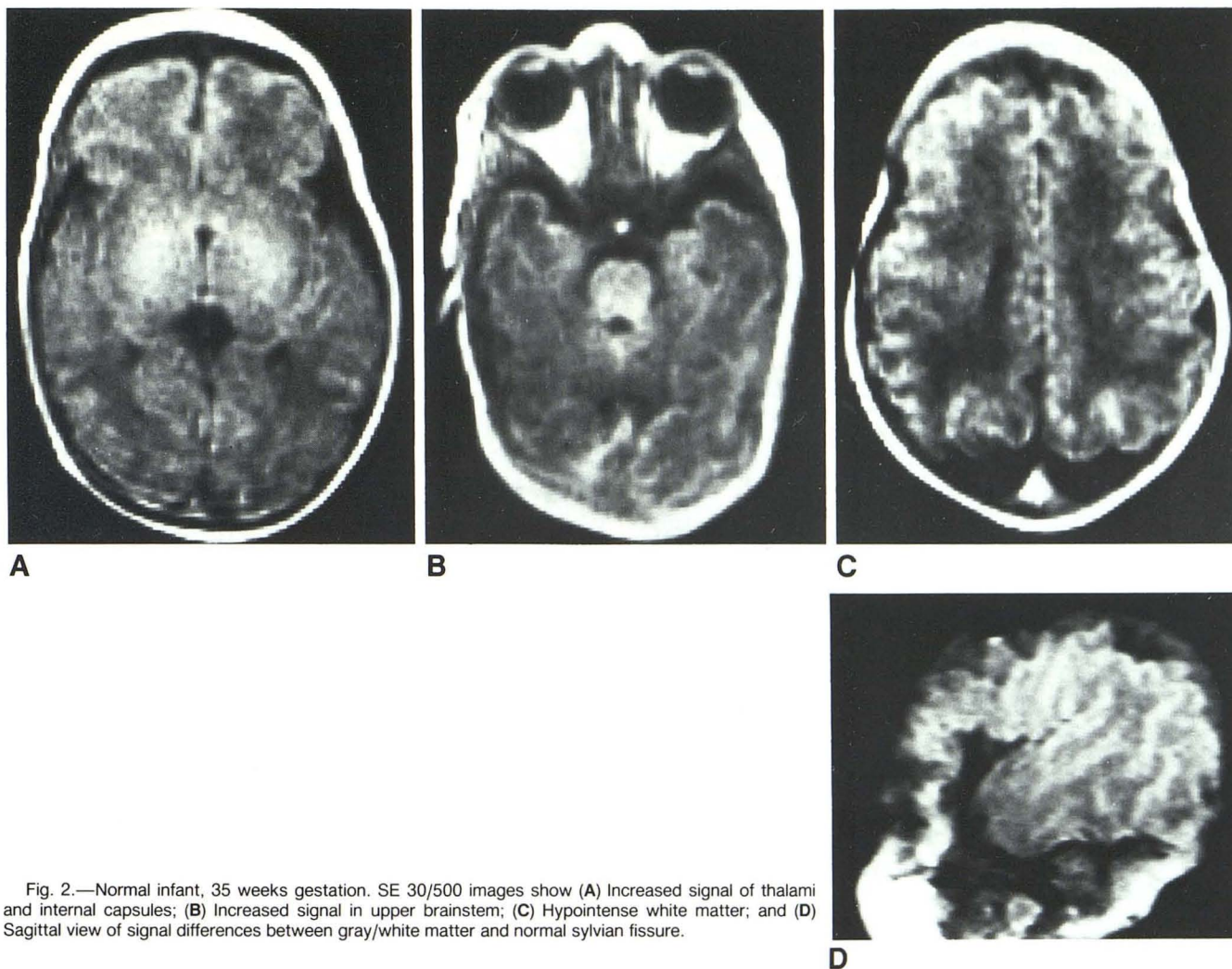
Fig. 2.—Normal infant, 35 weeks gestation. SE 30/500 images show (**A**) Increased signal of thalami and internal capsules; (**B**) Increased signal in upper brainstem; (**C**) Hypointense white matter; and (**D**) Sagittal view of signal differences between gray/white matter and normal sylvian fissure.

Spinal Lesions

Tethered cord (three cases). The spinal cords were tethered to the sacral sac and associated with lipomas in two cases (Fig. 22). One of these had a central midline region of hypointensity, presumably representing a diastematomyelia (Fig. 23). The third case was not associated with either abnormality.

Postradiation change (one case). The conus medullaris was deviated to one side after radiation to an associated neuroblastoma (Fig. 24). This was presumed to be secondary to arachnoiditis, as the appearances on repeated follow-up myelography performed in the 18 months prior to the MR scan were unchanged.

Discussion

Normal

Published reports [6–8] based on postmortem staining techniques indicate that myelination of the white matter begins at the caudal spinal cord as early as 20 weeks of gestation and proceeds rostrally to reach the internal capsules

and thalami at 36 weeks. The occipital white matter is myelinated at term, and the frontal lobes and intracortical association fibers are myelinated 3 months after birth.

The white matter of the premature brain appears hypointense compared with gray matter on T1-weighted images. Differences in protein, rather than in water content, are said to account for gray/white matter differentiation on CT scans [9–14]. The MR images of infants' brains in this age group show analogous appearances in that the white matter has a decreased signal compared with gray matter on T1-weighted sequences. The exact explanation of such appearances is complex, as the decreased signal due to lack of myelination is influenced by differences in protein content in the white matter as compared with the gray matter. Relaxation times of brains in this age group are not well documented compared with those of mature brains [15].

Myelination is detected on MR scanning because of the characteristic short T1 relaxation [16]. Inversion recovery is the optimal technique, and it is heavily T1-weighted. Spin-echo techniques using short TE and TR are routinely used in clinical MR imaging but are not as heavily T1 dependent.

Using the latter technique we are able to clearly demonstrate myelination of the internal capsule and thalami between 32 and 36 weeks gestation, and more extensive myelination of the occipital lobes by full term. The time and distribution of myelination in our patients correspond closely to those reported in postmortem studies [6–8], although there appear to be differences between subjects of the same gestational age. The detection of myelination earlier than that reported by Johnson [16] is probably related to individual differences. A greater number of scans of normal infants at different gestational ages is required to establish the normal range of myelination times.
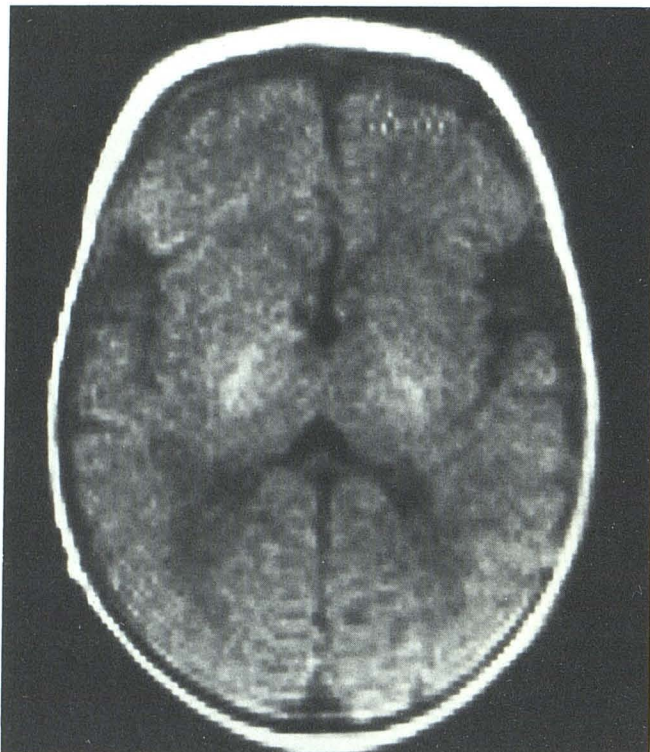

Fig. 3.—Normal infant, 37 weeks gestation. SE 30/500 image shows increased signal in posterior limbs of internal capsules.

Fig. 5.—Normal infant full term. SE 30/500 image shows increased signal in internal capsules only. Note small size of sylvian fissure (arrows).
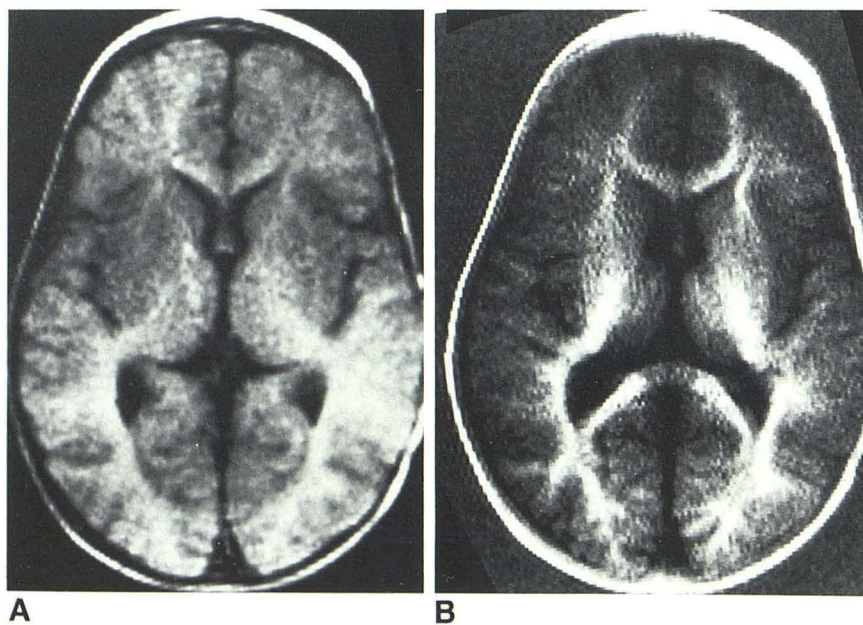

A   **B**

Fig. 4.—Normal infant, full term. SE 30/500 image (A) and IR 450/1500 image (B) show increased signal in white matter, more pronounced in thalami and occipital lobes than in frontal lobes.

The brains of infants appear to be isointense on T2-weighted SE images, unlike those of older children and adults, in whom the white matter is hypointense relative to the gray matter. This is probably related to the degree of myelination, which is not completed until adolescence [7, 8]. Incompletely myelinated neurons have less lipid content but more free water content compared with fully myelinated fibers. The contrary effects of these two components on white-matter T2 relaxation probably results in a signal intensity that is indistinguishable from that of gray matter.

The sylvian fissure forms as early as 15 weeks of gestation, becoming larger until sulci form in the remainder of the brain 5 weeks later [14]. It is markedly larger in the premature brain compared with the brain at full term. The inferior temporal sulcus forms at 32 weeks and is the last to develop before birth. The size of these fissures may be used to determine gestational age of the brain when correlated with the appear-

Fig. 6.—Normal infant, 20 months old. SE 30/500 image shows increased signal throughout entire white matter.
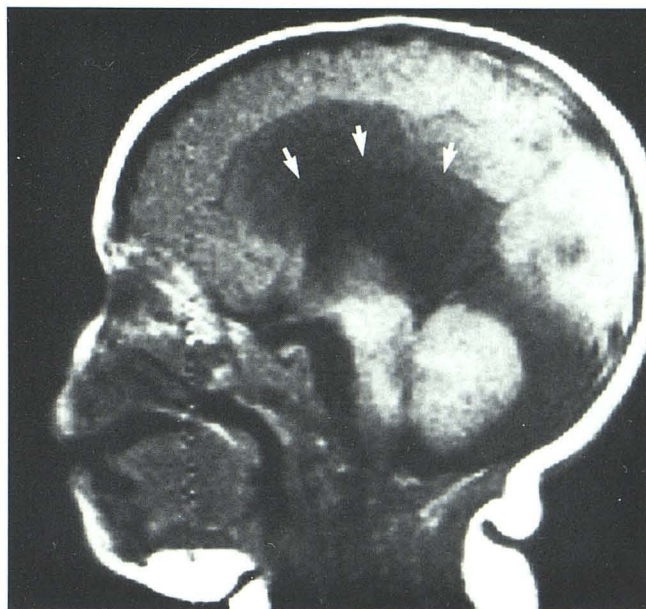

Fig. 8.—Corpus callosal agenesis. SE 30/500 image. Sagittal view shows absence of corpus callosum (arrows). Note hypoplastic cerebellum.
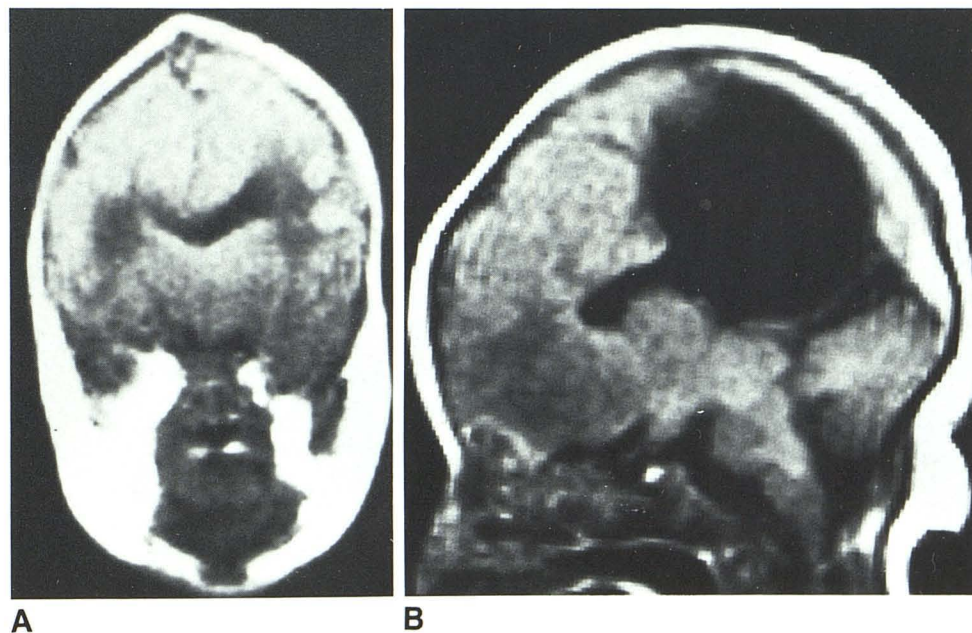

Fig. 7.—Alobar holoprosencephaly. SE 30/500 images. A, Coronal view shows single ventricle, absent falx, and interhemispheric fissure. B, Sagittal view shows large supratentorial dorsal sac, inseparable from posterior portion of ventricle.

A   B

ance of the white matter. The sagittal view will be invaluable in diagnosing abnormal gyral development, such as lissencephaly and micro- and macrogyria [14].

Congenital Abnormalities

MR is well able to evaluate midline defects such as holoprosencephaly, corpus callosal agenesis, Dandy-Walker defect, and midline cysts because of its ability to obtain both sagittal and coronal views. Alobar holoprosencephaly is associated with absence of the falx and a large dorsal sac [17, 18]. The corpus callosum is seldom visualized directly by CT or sonography, and agenesis is diagnosed by associated deformity of the ventricles. This structure is routinely deline-

ated in sagittal MR views by virtue of high spatial resolution and the slight difference in signal intensity between this structure and the rest of the white matter. Even slight hypoplasia of a portion of the corpus callosum may thus be accurately visualized on MR. The associated ventricular defects are seen as well on MR as on CT and sonographic scans [15–19]. Dandy-Walker and other midline cysts are usually visualized on sagittal CT and sonographic scans [20–23]. Occasionally

Fig. 9.—Gyral hypoplasia. SE 30/500 image. Sagittal view shows poorly developed sylvian fissure and cortical sulci.
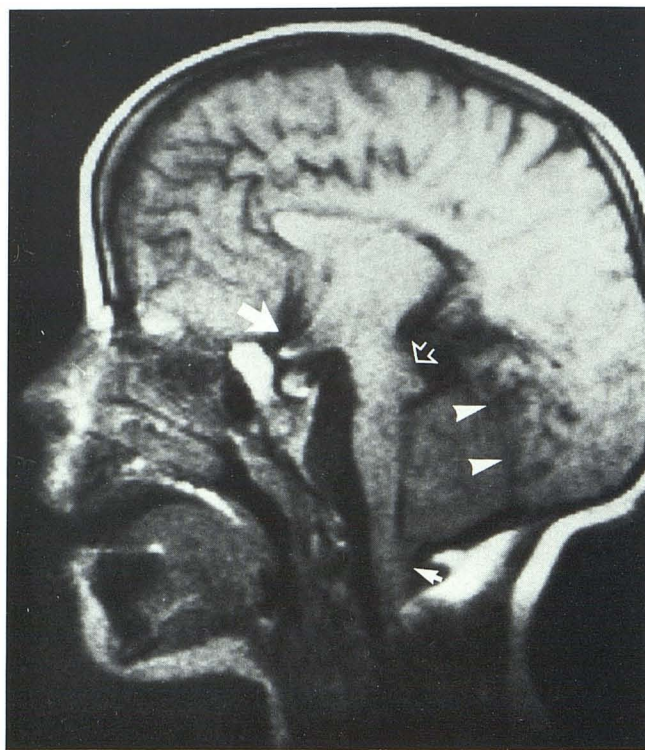

Fig. 11.—Arnold-Chiari malformation. SE 30/500 image. Sagittal view shows low-lying tonsils (*small arrow*), small posterior fossa, vertical tentorium (*arrowheads*), beak-shaped quadrigeminal plate (*open arrow*), and abnormal anterior recesses of third ventricle (*large arrow*).

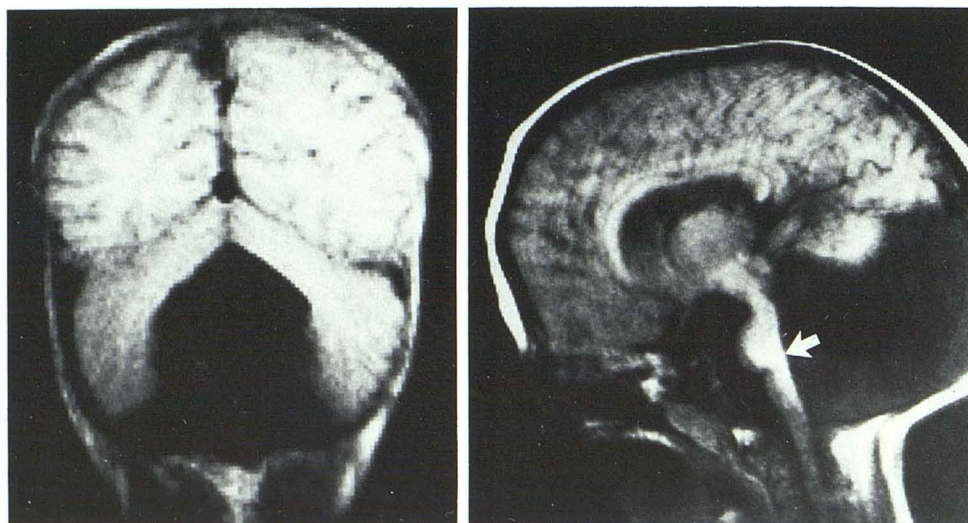A   B

Fig. 10.—Dandy-Walker malformation. SE 30/500 images. **A**, Coronal view shows giant fourth ventricle. **B**, Sagittal view shows absent vermis. Note brainstem hypoplasia (*arrow*).

Fig. 12.—Midline arachnoid cyst. SE 30/500 images. **A**, Coronal view shows large midline cyst displacing lateral ventricles (*arrows*) and extending through tentorial opening into posterior fossa. **B**, Sagittal view shows degree of extension into posterior fossa.
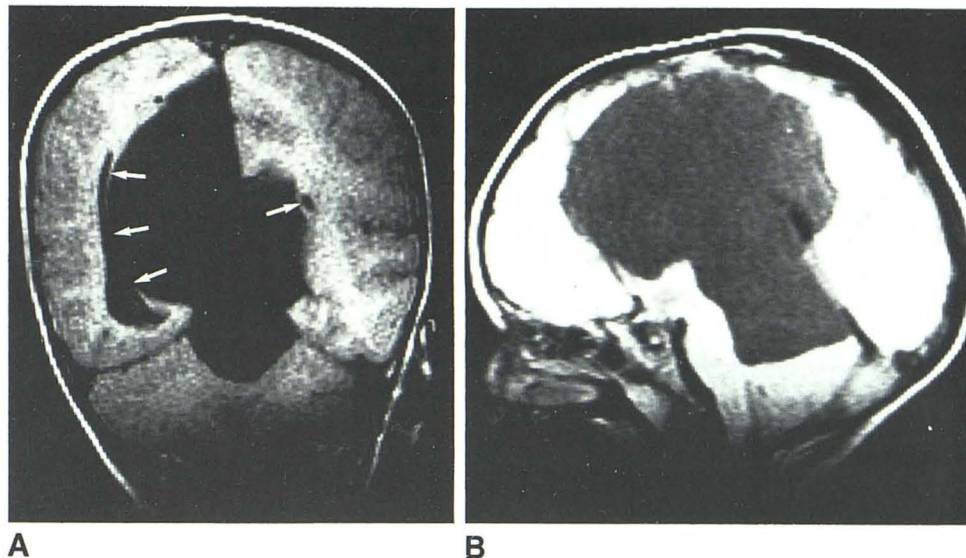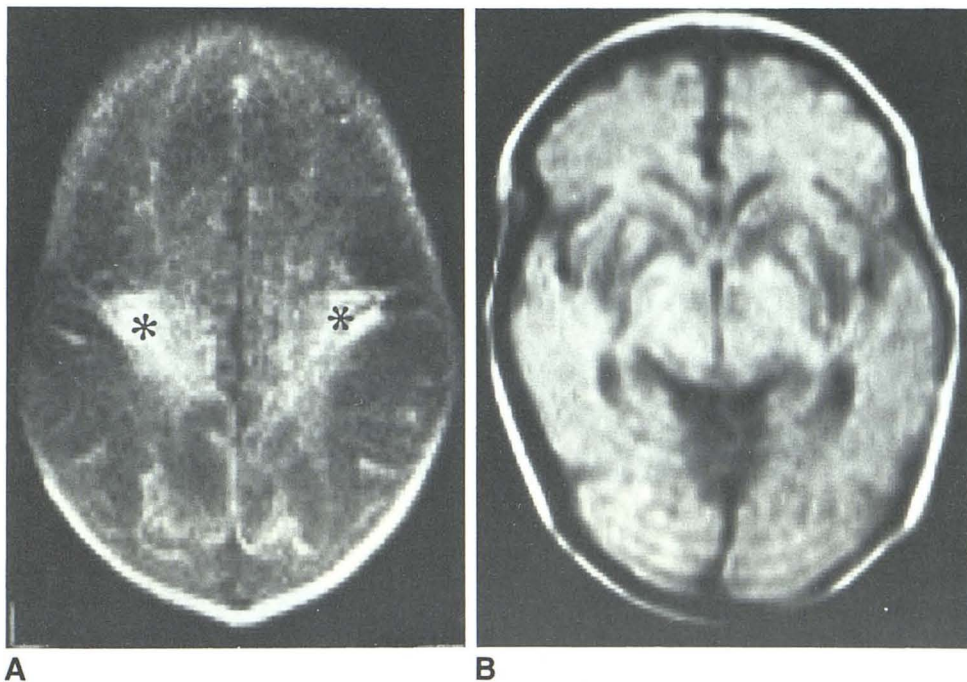
Fig. 13.—Anoxia, full-term infant. **A**, SE 30/500 image shows decreased signal in white matter, with focal increased signal in frontoparietal lobes (*asterisks*). **B**, SE 90/2000 image shows bilateral regions of decreased signal in basal ganglia.

it is not possible to differentiate cysts from dilated subarachnoid spaces. The signal intensity of fluid within cystic structures depends on the protein content, so that it is easy to differentiate true CSF-containing structures, which have less signal than loculated proteinaceous cysts. The sagittal and coronal views are especially useful in delineating the relationship of the fluid cavities to normal brain structures.

The Arnold-Chiari abnormality is shown much better on sagittal MR than on CT and sonography [24], allowing the precise configuration of the posterior fossa structures and degree of tonsillar ectopia to be evaluated. The abnormal commissures and recesses of the third ventricle can also be seen on MR scans.

Hydrocephalus is differentiated from atrophy by the rela-

tively normal size of the cortical gyri and the presence of periventricular increased signal on T2-weighted MR images, implying increased transependymal CSF absorption. The precise site of obstruction within the ventricular system, such as at the aqueduct, can be determined with certainty in most cases.

Perinatal Lesions

Anoxia. Acute anoxia may affect the watershed regions or be more generalized, and lesions may be visible as decreased attenuation on CT scans. It has been reported that the CT signs of decreased attenuation in premature anoxic infants correlate poorly with areas of ischemia and infarction on

autopsy [25]. Generalized decreased attenuation with compression of ventricles is more commonly seen with pathologically proved cerebral edema in anoxic full-term infants [25–27]. Severe anoxia results in brain destruction, which may be generalized or multifocal, and involve the white matter or the basal ganglia [28, 29]. The MR appearances of the white matter are similar to those seen on CT scans. Further experience with infants is required to determine if MR is more sensitive in detecting ischemic areas that are not seen on CT scans.
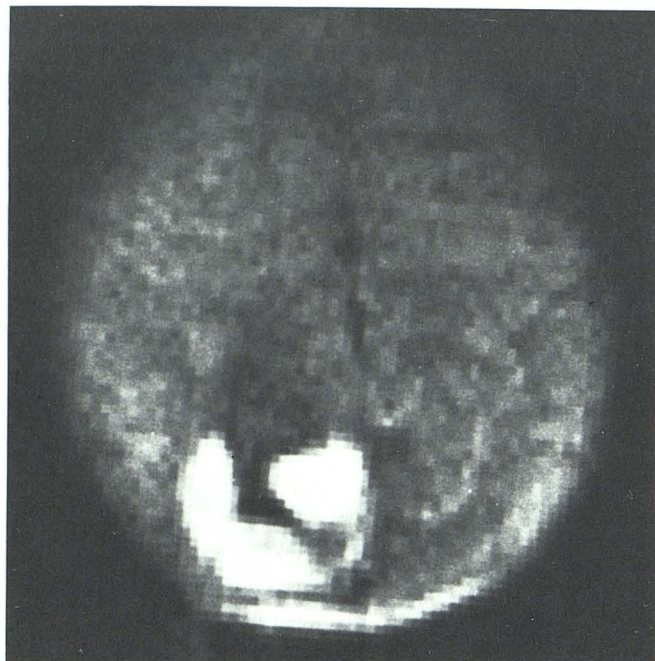
Hemorrhage. The locations of germinal matrix and intraventricular hemorrhages are different from those associated with anoxia of mature infants [30–34]. These hemorrhages are well demonstrated on sonography, CT, and MR [35–38]. Hematomas usually are easily detected on MR. The signal intensity depends on the age as well as the location of the hematomas. Acute hematomas are isointense and subsequently become hyperintense on account of short T1 relaxations resulting from the paramagnetic effect of methemoglobin [39]. A confident diagnosis of hematoma can thus only be

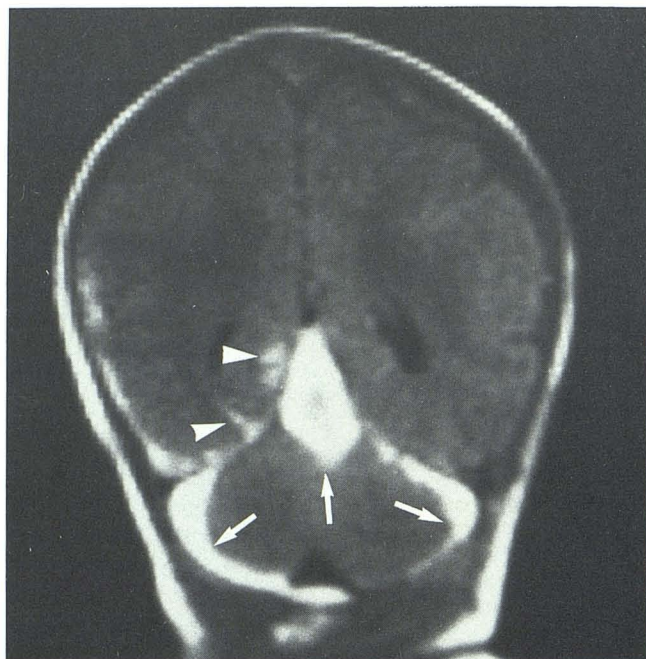Fig. 14.—Intracerebral hemorrhage. SE 30/500 image shows increased signal in right occipital lobe.

Fig. 15.—Subdural and subarachnoid hemorrhage, full-term infant. SE 30/500 image shows increased signal over cerebellar hemispheres, in quadrigeminal region (*arrows*), and on surface of right temporal lobe with extension into the sulci (*arrowheads*).
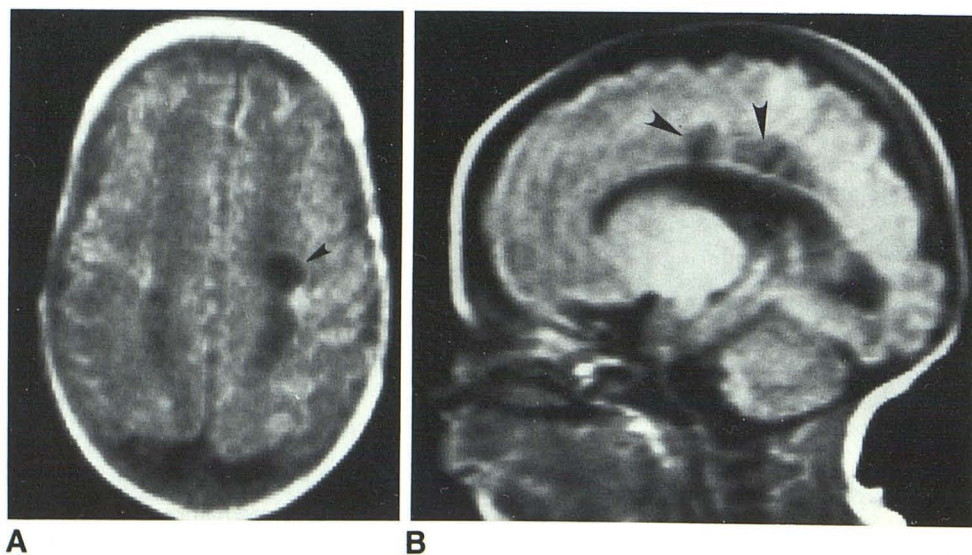

A   **B**

Fig. 16.—Periventricular leucomalacia, 36 weeks gestation. SE 30/500 images. Axial (**A**) and sagittal (**B**) views show multiple areas of decreased signal adjacent to lateral ventricles (*arrowheads*).

Fig. 17.—Cerebral hemiatrophy, 2 years old. **A,** SE 30/500 image shows focal atrophy with dilated sulci (*arrowheads*), cystic decreased signal in white matter (*arrow*), and ventricular dilatation (*asterisk*). **B,** SE 90/2000 image shows a larger region of increased signal in white matter. Note hemiatrophy of entire ipsilateral hemisphere.
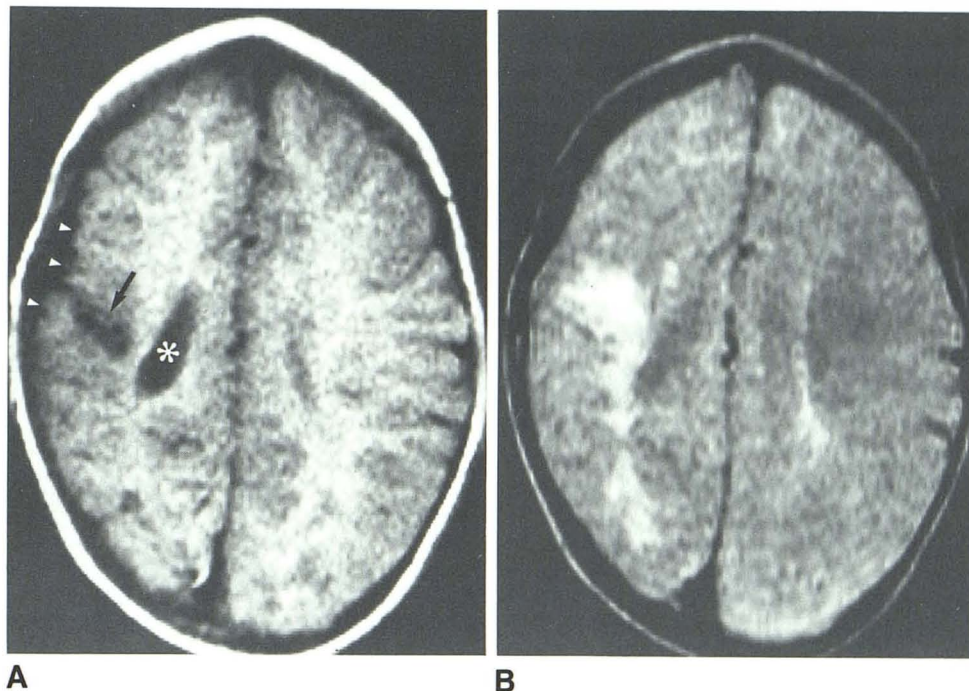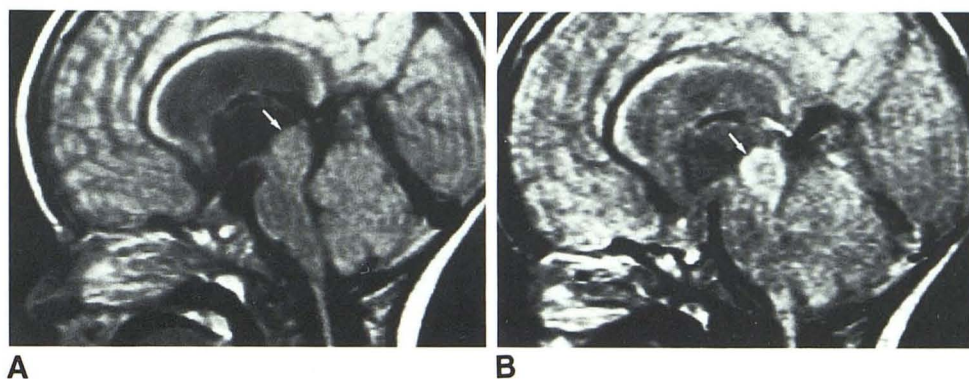

A   B

Fig. 18.—Pineal tumor, 6 weeks old. **A,** SE 30/500 image. Sagittal view shows large isointense pineal mass with compression of aqueduct (*arrow*). **B,** SE 90/2000 image. Sagittal view shows slightly increased signal of pineal tumor (*arrow*). Hydrocephalus is present.

A   B

made when the characteristic hyperintense signal is detected on T1 images; the T2 changes on the other hand are entirely nonspecific.

An advantage of MR is the precise localization of the sites of hematoma, particularly those of extracerebral origin. In a case in which the location and origin of the hemorrhage was in doubt, MR showed the hemorrhage to be present in the quadrigeminal region and in the posterior fossa, but not in the basal cisterns. The appearances favored subdural rather than subarachnoid locations of the hemorrhage. The difference in the signal intensity of the blood in the quadrigeminal region probably represented different stages of resolution.

Periventricular leukomalacia following intraventricular [40, 41] hemorrhages are well shown by MR. The damage to the white matter in this condition is more readily evaluated on MR. Comparison with myelination of normal brains of the same gestational age may reveal changes not detected on CT.

Hemiatrophy and atrophy secondary to infarction are well shown on T1-weighted images. A large area of abnormal signal on T2-weighted images in the same location in our case (see Fig. 20) probably represented extensive demyelination resulting from the initial infarct.

Other Lesions

The calcified tubers are visible on MR (see Fig. 21) but not as clearly as on CT [42, 43]. They are visible as isointense nodules, presumably because of the contrary effect of increased signal of the soft-tissue component and calcium of the tubers. Noncalcified white-matter changes are probably better seen on MR than on CT. Based on the limited experience in this study, it is not possible to determine what role MR will play in evaluating this disorder.

Tumors. Congenital intracranial tumors are uncommon, and they often present with minimal clinical symptoms and signs. Pineal tumors usually cause hydrocephalus, and are easily differentiated from benign aqueductal stenosis by their mass effect and characteristic signal intensities reflecting long T1

and T2 relaxations [44–46]. Optic chiasm gliomas are extremely well delineated on sagittal MR views. Spread of the tumor along the entire optic pathways, often poorly seen on CT, is sometimes detected as increased signal on T2-weighted images [47]. Craniopharyngiomas are usually cystic [48–50]. The size and location of the tumor is well delineated, but the signal of the cystic fluid is usually nonspecific and dependent on the protein and cholesterol content. The relationship of this tumor to the pituitary gland is clearly defined.

Spinal Lesions

The spinal cord and conus medullaris are visualized on MR, though not with as much detail as on myelography [51–54].

Lipomas have characteristic signal reflecting short T1 relaxation; and other lesions, such as diastematomyelia, are adequately visualized without need for intrathecal contrast studies. Changes in position of the conus medullaris secondary to arachnoiditis may be evaluated. The lack of abnormal signal on T2-weighted images in such cases is a useful indication of a benign process, as most intrinsic tumors exhibit increased signal compared with the normal spinal cord [55]. MR is
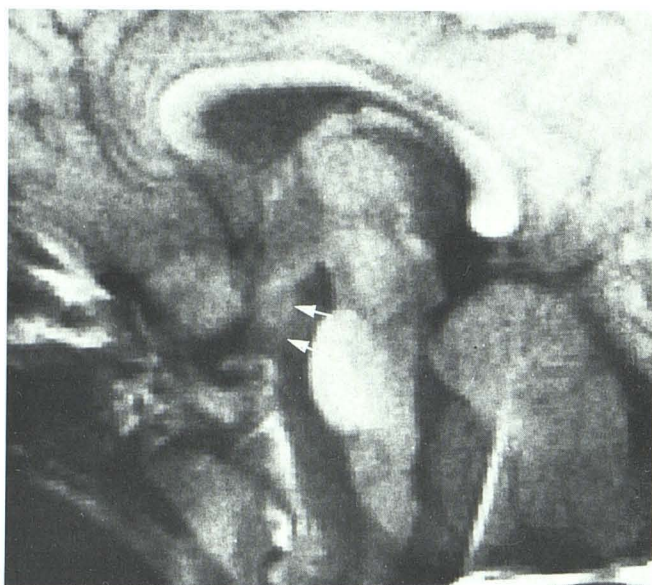

Fig. 19.—Optic chiasm glioma. SE 30/500 image. Sagittal view shows large isointense mass obliterating suprasellar cistern (*arrows*). Optic chiasm and pituitary stalk are not identified.
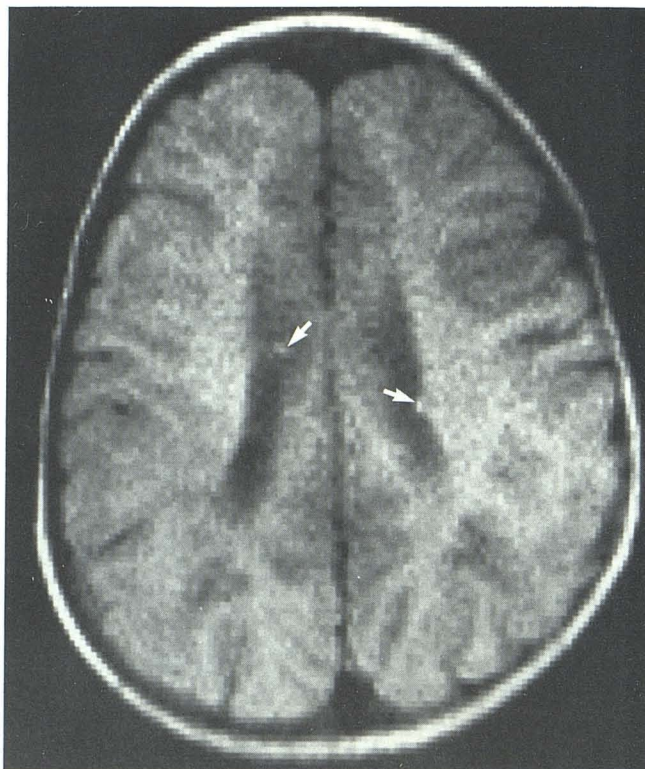
Fig. 21.—Tuberose sclerosis, 4 years old. SE 30/500 image shows isointense calcified subependymal nodules (*arrows*).
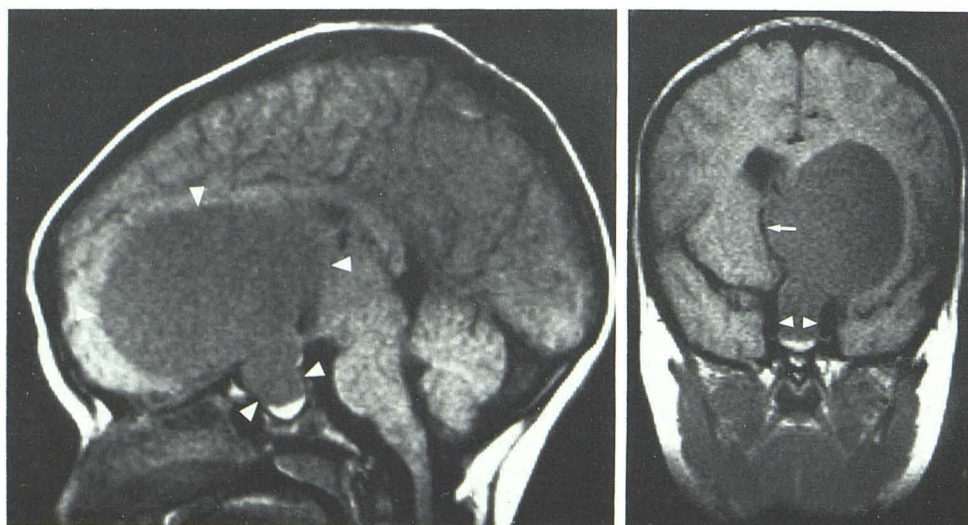
A   B

Fig. 20.—Craniopharyngioma. SE 30/500 image. **A**, Sagittal view shows large frontal cyst extending into an enlarged sella (*arrowheads*). **B**, Coronal view shows cyst in left frontal region displacing anterior cerebral artery branches across midline (*arrow*). Note relation of cyst to carotid arteries (*arrowheads*) and pituitary gland.

22   **23**   **24**

Fig. 22.—Lipoma/tethered cord, 2 years old. SE 30/500 image. Sagittal view shows conus medullaris adherent to a region of hyperintense signal (*arrows*). The spinal canal is large.

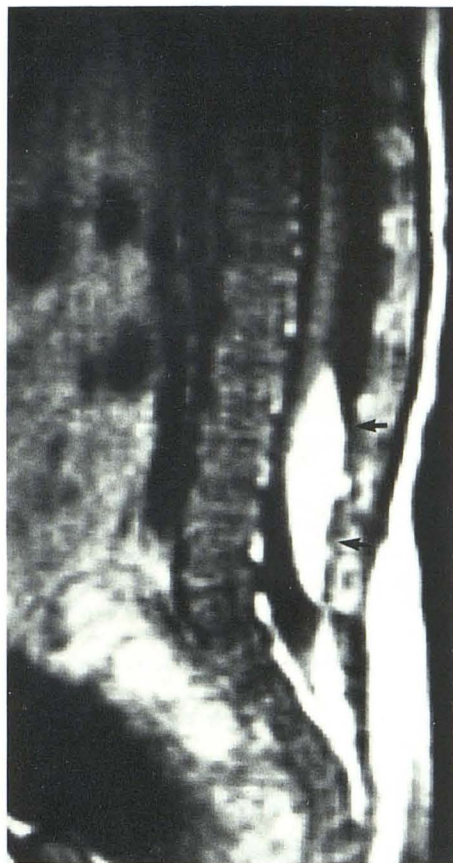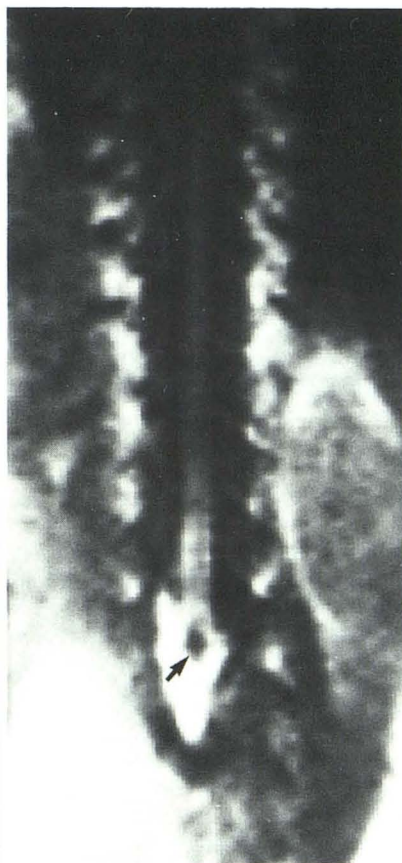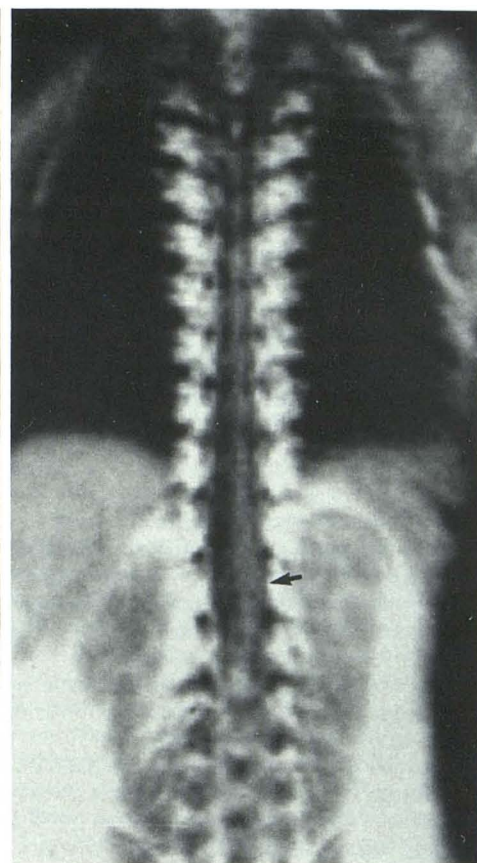Fig. 23.—Lipoma and diastematomyelia. SE 30/500 image. Coronal view shows filling defect within a lipoma (*arrow*).

Fig. 24.—Postradiation change. SE 30/500 image. Coronal view shows deviation of conus medullaris to left (*arrow*).

undoubtedly a good initial examination, and may well replace myelography as the method of choice for evaluating spinal cord abnormalities in young children.

REFERENCES

1. Grant EG, Schellinger D, Borts FT, et al. Real-time sonography of the neonatal and infant head. *AJNR* **1980**;1:487–492, *AJR* **1981**;136:265–270
2. Rumack CM, Johnson ML. *Perinatal and infant brain imaging*. Chicago: Year Book Medical Publishers, **1984**
3. Wolff S, Crooks LE, Brown P, Howard R, Painter RB. Tests for DNA and chromosomal damage induced by nuclear magnetic resonance imaging. *Radiology* **1980**;136:707–710
4. Thomas A, Morris PG. The effects of NMR exposure on living organisms. I. A microbial assay; II. A genetic study of human lymphocytes. *Br J Radiol* **1981**;54:615–625
5. Gerard CR, Osmark RS, Hall EJ, et al. Magnetic resonance and ionizing radiation: a comparative evaluation in vitro of oncogenic and genotoxic potential. *Radiology* **1984**;152:192–202
6. Larroche JC. *Developmental pathology of the neonate*. Amsterdam: Excepta Medica, **1977**
7. Yakoalev PI, Lecours AR. The myelogenetic cycles of regional maturation in the brain. In: Minkowski A, ed. *Regional develop-*

ment of the brain in early life. Oxford: Blackwell Scientific Publications, **1967**:3–10
8. Le Mire RJ, Loeser JD, Leach RW, Alvord EC. *Normal and abnormal development of the human nervous system*. New York: Harper & Row, **1977**:2–13, 42–45
9. Arimitsu T, DiChiro G, Brooks RA, Smith PB: White-gray matter differentiation in computed tomography. *J Comput Assist Tomogr* **1977**;1:437–442
10. Picard L, Claudon M, Roland J, et al. Cerebral computed tomography in premature infants, with an attempt at staging developmental features. *J Comput Assist Tomogr* **1980**;4(4):435–444
11. Brant-Zawadzki M, Enzmann DR. Using computed tomography of the brain to correlate low white-matter attenuation with early gestational age in neonates. *Radiology* **1981**;139:105–108
12. Suzuki K. Chemistry and metabolism of brain lipids. In: Ford DE, ed. *Neurobiological aspects of maturation and aging*. Progress in Brain Research Series. New York: Elsevier, **1973**:40:312
13. Norton WT. Formation, structure and biochemistry of myeline. In: Siegel GJ, Alberts RW, Katzman R, et al., eds. *Basic neurochemistry*. 2nd ed. Boston: Little, Brown, **1976**:7
14. Le Mire RJ, Loeser JD, Leech RW, Alvord EC. *Normal and abnormal development of the human nervous system*. New York: Harper & Row, **1977**:233–239
15. Hutchinson JMS, Smith FW. NMR clinical results: Aberdeen. In: Partain CL, James AE, Rollo FD, Price RR, eds. *Nuclear magnetic*

resonance (NMR) imaging. Philadelphia: Saunders, **1983**:238–239

16. Johnson MA, Pennock JM, Bydder GM, et al. Clinical NMR imaging of the brain in children: normal and neurologic disease. *AJNR* **1983**;4:1013–1026

17. Probst FB. The prosencephalies. In *Morphology, neuroradiological appearances and differential diagnosis*. Berlin: Springer-Verlag, **1979**

18. Byrd SE, Harwood-Nash DC, Fitz CR, Rogovitz DM. Computed tomography evaluation of holoprosencephaly in infants and children. *J Comput Assist Tomogr* **1977**;1:456–463

19. Byrd SE, Harwood-Nash DC, Fitz CR. Absence of the corpus callosum: computed tomographic evaluation in infants and children. *J Can Assoc Radiol* **1978**;29:108–112

20. Archer CR, Darwish H, Smith K Jr. Enlarged cisternae magnae and posterior fossa cysts simulating Dandy-Walker syndrome on computed tomography. *Radiology* **1978**;127:681–689

21. Naidich TP, Leeds NE, Kircheff II, et al. The tentorium in axial section. I. Normal CT appearance and nonneoplastic pathology. *Radiology* **1977**;123:631–638

22. Juhl JH, Wesenber M. Computed tomography of the enlarged cisterna magna. *Radiology* **1979**;131:385–391

23. Mori K, Hayashi T, Handa H. Radiological manifestations of infratentorial retrocerebellar cysts. *Neuroradiology* **1977**;123:631–638

24. Naidich TP, Pudlowski RM, Naidich JB, et al. Computed tomographic signs of the Chiari II malformation. *Radiology* **1980**;134:65–75,391–398,657–663

25. Flodmark O, Becker LE, Harwood-Nash DC, et al. Correlation between computed tomography and autopsy in premature and full-term neonates that have suffered perinatal asphyxia. *Radiology* **1980**;137:93–103

26. Hirabayashi S, Kitahara T, Hishida T. Computed tomography in perinatal hypoxic and hypoglycemic encephalopathy with emphasis on follow-up studies. *J Comput Assist Tomogr* **1980**; 4:445–450

27. Magilner AD, Wertheimer IS. Preliminary results of computed tomography study of neonatal brain hypoxia-ischemia. *J Comput Assist Tomogr* **1980**;14(4):457–463

28. Voorhies TM, Lipper EG, Lee BCP, Vanucci RL, Auld PAM. Occlusive vascular disease in asphyxiated newborn infants. *J Pediatr* **1984**;104:92–96

29. Kotagal S, Tore SS, Kotagal P, Archer CR. Symmetrical bithalamic and striatal hemorrhage following perinatal hypoxia in a term infant. *J Comput Assist Tomogr* **1983**;7:353–355

30. Pevsner PH, Garcia-Bunnel R, Leeds N, Finklestein M. Subependymal and intraventricular hemorrhages in neonates: early diagnosis by computed tomography. *Radiology* **1976**;119:111–114

31. Burstein J, Papile L, Burstein R. Subependymal germinal matrix and intraventricular hemorrhage in premature infants: diagnosis by CT. *AJR* **1977**;128:971–976

32. Burstein J, Papile L, Burstein R. Intraventricular hemorrhage and hydrocephalus in premature newborns: a prospective study with CT. *AJR* **1979**;132:631–635

33. Lee BCP, Grassi AE, Schechner S, Auld PAM. Neonatal intraventricular hemorrhage: a serial computed tomography study. *J Comput Assist Tomogr* **1979**;132:631–635

34. Flodmark O, Fitz CR, Harwood-Nash DC. CT diagnosis and short term prognosis of intracranial hemorrhage and hypoxic/

ischemic brain damage in neonates. *J Comput Assist Tomogr* **1980**;4:775–787

35. Grant EG, Borts FT, Schellinger D, McCullough DC, Sivasubramian KN, Smith Y. Real-time ultrasonography of neonatal intraventricular hemorrhage and comparison with CT. *Radiology* **1981**;139:687–691

36. Grant EG, Borts FT, Schellinger D, et al. Cerebral intraparenchymal hemorrhage in neonates: sonographic appearance. *AJNR* **1981**;2:129–132

37. Sipponen JT, Sipponen RE, Sivula A. Nuclear magnetic resonance (NMR) imaging of intracerebral hemorrhage in the acute and resolving phases. *J Comput Assist Tomogr* **1983**;7:954–959

38. DeLaPaz RL, New PFJ, Buonanno FS, et al. NMR imaging of intracranial hemorrhage. *J Comput Assist Tomogr* **1984**;8:599–604

39. Bradley WG Jr, Schmidt PG. Effect of methemoglobin formation on the MR appearance of subarachnoid hemorrhage. *Radiology* **1985**;156(1):99–103

40. Di Chiro G, Arimitsu T, Pellock JM, Landers RD. Periventricular leukomalacia related to neonatal recognition by computed tomography. *J Comput Assist Tomogr* **1978**;2:352–354

41. Grant EG, Kerner M, Schellinger D, et al. Evolution of porencephalic cysts from intraparenchymal hemorrhage in neonates: sonographic evidence. *AJNR* **1982**;3:47–50

42. Lee BCP, Gawler G. Tuberous sclerosis. *Radiology* **1978**; 127:403–407

43. Gomez MR, ed. *Tuberous sclerosis*. New York: Raven Press, **1979**

44. Dupont MG, Gerard JM, Flament-Durand J, et al. Pathognomic aspect of germinoma on CT scan. *Neuroradiology* **1977**;14:209–211

45. Zimmerman RA, Bilaniuk LT, Wood JH, et al. Computed tomography of pineal, parapineal, and histologically related tumors. *Radiology* **1980**;137(3):669–677

46. Futrell NN, Osborn AG, Cheson BD. Pineal region tumors: computed tomographic-pathologic spectrum. *AJNR* **1981**;2:415–420

47. Albert A, Lee BCP, Saint-Louis L, Deck MDF. MRI of optic chiasm and optic pathways. *AJNR* **1986**;7:255–258

48. Fitz CR, Wortzman G, Harwood-Nash DC, et al. Computed tomography in craniopharyngiomas. *Radiology* **1978**;22:39–42

49. Kitano I, Yoneda K, Yamakawa Y, et al. Huge cystic craniopharyngioma with unusual extensions. *Neuroradiology* **1981**;22:39–42

50. Braun IF, Pinto RS, Epstein F. Dense cystic craniopharyngiomas. *AJNR* **1982**;3:139–141

51. Han JS, Kaufman BS, Youssef SJ, et al. NMR imaging of the spine. *AJNR* **1983**;4:1151–59

52. Norman D, Mills CM, Brant-Zawadzki M, et al. Magnetic resonance imaging of the spinal cord and canal: potential and limitations. *AJNR* **1984**;5:9–14

53. Modic MT, Weinstein MA, Pavlicek W, et al. Magnetic resonance imaging of the cervical spine: technical and clinical observations. *AJNR* **1984**;5:15–22

54. Lee BCP, Manning JJ, Deck MFD. MR imaging of syringomyelia and hydromyelia. *AJNR* **1985**;6:221–228

55. DiChiro G, Doppman JL, Dwyer AJ, et al. Tumor and arteriovenous malformation of the spinal cord: assessment using MR. *Radiology* **1985**;156:689–698